J Sol-Gel Sci Technol (2015) 75:593–601
DOI 10.1007/s10971-015-3730-4

ORIGINAL PAPER

Structural characterisation of slightly Fe-doped $SrTiO_3$ grown via a sol–gel hydrothermal synthesis

S. Fuentes[1,5] · P. Muñoz[1] · N. Barraza[2] · E. Chávez-Ángel[3] · C. M. Sotomayor Torres[3,4]

Received: 8 April 2015 / Accepted: 30 April 2015 / Published online: 16 May 2015
© Springer Science+Business Media New York 2015

Abstract A detailed structural study of the incorporation of Fe into $SrTiO_3$ nanoparticles is reported. Slightly iron-doped strontium titanate nanoparticles with 0, 1, 3 and 5 mol% concentration of iron were grown using a sol–gel hydrothermal process and characterised using Raman scattering, X-ray photoelectron and X-ray diffraction spectroscopy. The amorphisation of the nanostructures was observed as the iron content increased, which was confirmed by the TEM images. The XPS results indicated that the oxidation states of the Sr atoms were maintained in 2+. However, a mixture of Fe^{3+} and Fe^{4+} atoms was observed as the Fe content increased, resulting in a significant number of oxygen vacancies in the perovskite structure. The analysis of Raman spectra indicated that the intensity, linewidth and frequency shift of the TO_4 phonon can be used as an indicator of the Fe content as well as a local temperature probe for future thermal analysis.

Graphical abstract Temperature evolution of the Raman spectra of STO:Fe 1 mol%. The peaks with star correspond to the second-order processes. (b) Temperature dependence of the TO_4 phonon mode. Blue dots denote measured Raman spectra, and the red solid lines are the Lorentzian fits to respective spectra.

✉ S. Fuentes
sfuentes@ucn.cl

✉ E. Chávez-Ángel
emigdio.chavez@icn.cat

[1] Departamento de Ciencias Farmacéuticas, Facultad de Ciencias, Universidad Católica del Norte, Casilla 1280, Antofagasta, Chile

[2] Departamento de Física, Facultad de Ciencias, Universidad de Santiago de Chile (USACH), Santiago, Chile

[3] Institut Catalá de Nanociencia i Nanotecnología (ICN2), Campus de la UAB, 08193 Bellaterra, Barcelona, Spain

[4] Institució Catalana de Recerca i Estudis Avançats (ICREA), 08010 Barcelona, Spain

[5] Center for the Development of Nanoscience and Nanotechnology (CEDENNA), Santiago, Chile

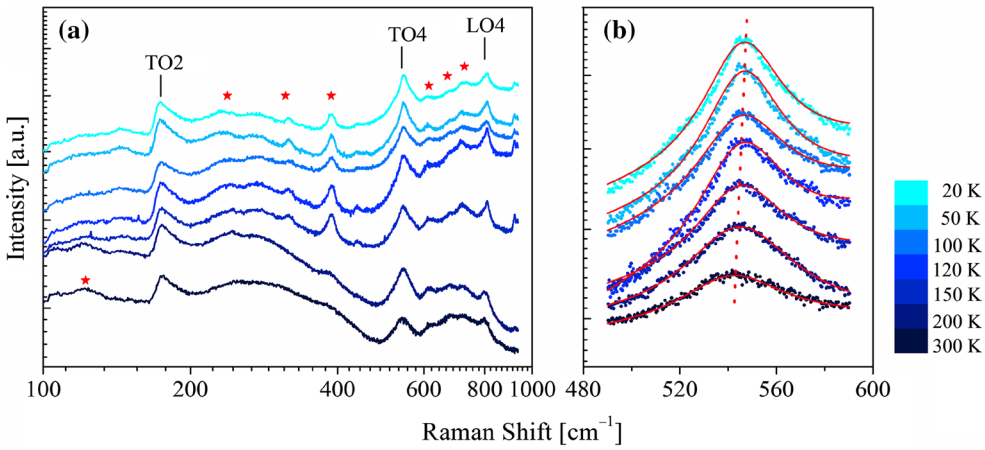

Keywords Strontium titanate · Fe-doped · Raman scattering · XPS analysis

1 Introduction

The perovskite-type oxides, which have a general formula of ABO_3, have been the focus of extensive research due to their outstanding properties ranging from high-temperature superconductivity to colossal magnetoresistance [1]. Among these oxides, strontium titanate (STO) has exhibited several promising features for application of this material in new electronic devices [2–9]. Its innumerable applications in many fields are due to its large nonlinear optical properties, extremely high and electric-field tuneable dielectric constant, energy storage ability, high thermal stability and photocatalytic properties [10–12].

However, the properties of STO are dependent on its chemical composition as well as its structure, shape and size [13, 14]. Other important characteristics of these materials include the partial substitution of the cations at both the A and B sites of ABO_3 and the ability to maintain the stability of unusual mixed oxidation states in the crystal structure. To obtain a high dielectric constant and semiconducting behaviour of devices based on STO, it is necessary to modify or tailor the crystal structure. This modification is typically accomplished by chemical substitution with transition metals and the promotion of defects (i.e. vacancy in the structure) [15, 16].

Fe-doped strontium titanate, $SrTi_{(1-x)}O_3$:Fe_x, is a continuous solid-state solution between strontium ferrite ($SrFeO_3$) and strontium titanate. Due to the difference in the oxidation states between the titanium (Ti^{4+}) and iron atoms (Fe^{3+}), oxygen vacancies are commonly observed in the Fe-doped strontium titanate compound, STO:Fe. In fact, the formation of oxygen vacancies maintains the charge balance [17–19]. This structural characteristic can be used to reduce the electrical resistance of the undoped STO and to engineer high-sensitivity oxygen sensors [20].

STO:Fe has been studied for its redox behaviour [15], photocatalytic activity [22] and nonlinear optical properties [18], as well as for use as a gas sensor material [21] and phase shifter in communication systems [23]. However, the STO:Fe compound is not well understood, and more research is needed.

To achieve a comprehensive understanding of the structure–property relationships in multiferroic materials, the study of phonon dynamics is crucial. For example, Raman scattering spectroscopy is an invaluable tool for studying the lattice dynamics of these systems due to its sensitivity to short-range distortions arising from microstructural defects.

Recently, a Raman study reported by Van Minh et al. [24] on STO:Fe indicated that a strong reduction in the broad structure characteristic of SrTiO3 in the 200–500 cm^{-1} region was observed as the iron concentration increased. In addition, the activation of a single peak at approximately 690 cm^{-1}, which is absent in undoped STO, was observed due to doping with Fe^{+4} ions [25].

In this study, the preparation of STO and $SrTi_{(1-x)}O_3$:Fe_x ($x = 0$, 1, 3 and 5 mol% Fe) using a sol–gel hydrothermal method is reported. Structural and surface chemistry analyses indicate that amorphisation occurs as the Fe content increases.

2 Experimental

2.1 Synthesis

$SrTi_{(1-x)}O_3$:Fe_x powders with $x = 0$, 1, 3 and 5 mol% Fe were synthesised by a sol–gel hydrothermal process using titanium tetrachloride ($TiCl_4$, 1 M, Aldrich), strontium

chloride ($SrCl_2 \cdot 6H_2O$, 99.999 %, Aldrich) and iron oxide (Fe_2O_3, Aldrich) as starting materials.

In a typical procedure, three different solutions were prepared as follows: solution (A) containing 7 mL of $TiCl_4$ was diluted with 2.3 mL of 2 M HCl to form a predominantly yellow solution; solution (B) was prepared by dissolving 2.4 g of $SrCl_2 \cdot 6H_2O$ in 4 mL of deionised water; and solution (C) was prepared by dissolving Fe_2O_3 in 2 mL of HCl.

The Fe-doped STO precursor was prepared by the dropwise addition of (A) and (B) into (C). Under stirring and N_2 bubbling, 13 mL of 6 M NaOH was added to the strontium iron titanium solution and a white homogeneous colloidal strontium iron titanium slurry was formed.

The mixed solution was transferred to a 100-mL Teflon-lined stainless steel reactor, which was sealed and heated at 180 °C for 24 h under an oxygen partial pressure of 35 bar. Finally, the autoclave was cooled to room temperature under environmental conditions. The as-synthesised white powder attached to the walls of the Teflon container was collected, centrifuged, washed with distilled water and ethanol to remove the remaining ions, and dried at 60 °C for 6 h under reduced pressure.

2.2 Characterisation

The surface chemistry of the STO:Fe samples was characterised by X-ray photoelectron spectroscopy (XPS; Physical Electronics system model 1257) using Al K_α emission. The binding energies and oxidation states were obtained from high-resolution scans. The energy scale was calibrated by assigning 284.8 eV to the C 1 s peak. X-ray diffraction (XRD) data were acquired using a Siemens Advanced D-8 diffractometer with CuK_α radiation at 40 kV and 30 mA. The Raman spectra were recorded with a T64000 Raman spectrometer manufactured by HORIBA Jobin–Yvon using the single grating mode (2400 lines) with a spectral resolution better than 0.4 cm^{-1}. The spectra were excited by a 2.5-mW laser with a wavelength of 514.5 nm. The temperature-dependent measurements were performed using an Oxford constant flow cryostat, which allowed for a variation of temperature from 20 to 300 K with ±1 K control. Transmission electron microscopy (TEM) studies were performed on a Jeol JEM-2011 operated at 200 kV in diffraction and phase-contrast modes.

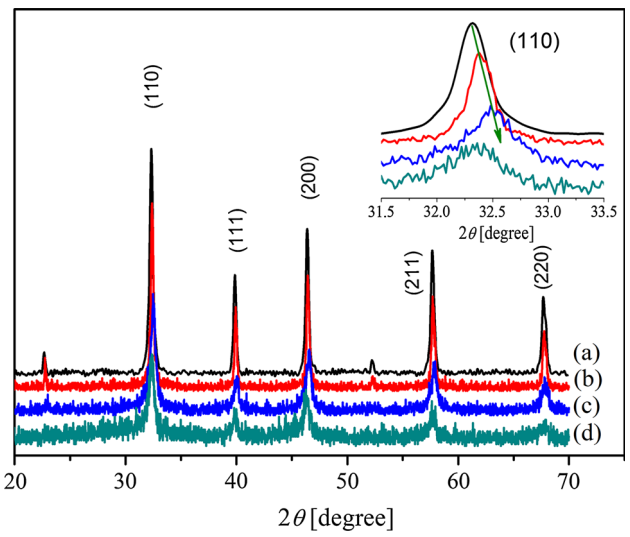

Fig. 1 XRD patterns of STO doped with different content of Fe: (*a*) 0, (*b*) 1, (*c*) 3 and (*d*) 5 mol%, respectively. The *inset* shows the 2θ region of 31° and 33°

3 Results

3.1 X-ray diffraction

Figure 1 shows the X-ray diffraction patterns of the STO and STO:Fe samples. These samples were not subjected to annealing. As shown in Fig. 1, the sharp and well-defined peaks indicated the high crystallinity of both the STO and Fe-doped STO samples at lower concentrations (1 mol%). The XRD Bragg reflection was assigned to the cubic perovskite structure of STO. In fact, all of the main peaks for the STO samples in Fig. 1 were stabilised in the cubic lattice (space group *Pm3m*), and the calculated lattice constants were consistent with the tabulated values ($a = 3.912$ Å; JCPDS card no. 73-0661). No diffraction peaks related to $SrCO_3$ or iron oxide phases were observed, which indicates that the iron ions were homogeneously incorporated in the STO lattice.

However, in comparison with pure STO, the relative peak intensity of the perovskite peaks decreased with increasing Fe concentrations, suggesting that the samples become less crystalline. The samples with higher Fe concentrations were primarily amorphous with a small degree of crystallisation.

The inset in Fig. 1 shows the XRD patterns of all of the samples in the 31°–33° 2θ range. A single-peak diffraction between 31° and 33° was observed corresponding to the (1 1 0) Bragg reflection. The effect of an increase in the Fe substitution on the STO structure was detected as a shift in the (1 1 0) reflection towards a higher diffraction angle. No double peaks were observed in the 45°–48° 2θ range, which is characteristic of the STO cubic lattice.

The XRD peaks shift to a higher diffraction angle with increasing Fe concentrations, which confirms the increasing substitutional doping of Fe in STO. The ionic radius of Fe^{3+} (0.585 Å) is smaller than that of Ti^{4+} (0.605 Å). Therefore, doping of Fe leads to decreased lattice parameters and interplanar spacing in STO. The Rietveld refinements of the XRD data were carried out using the

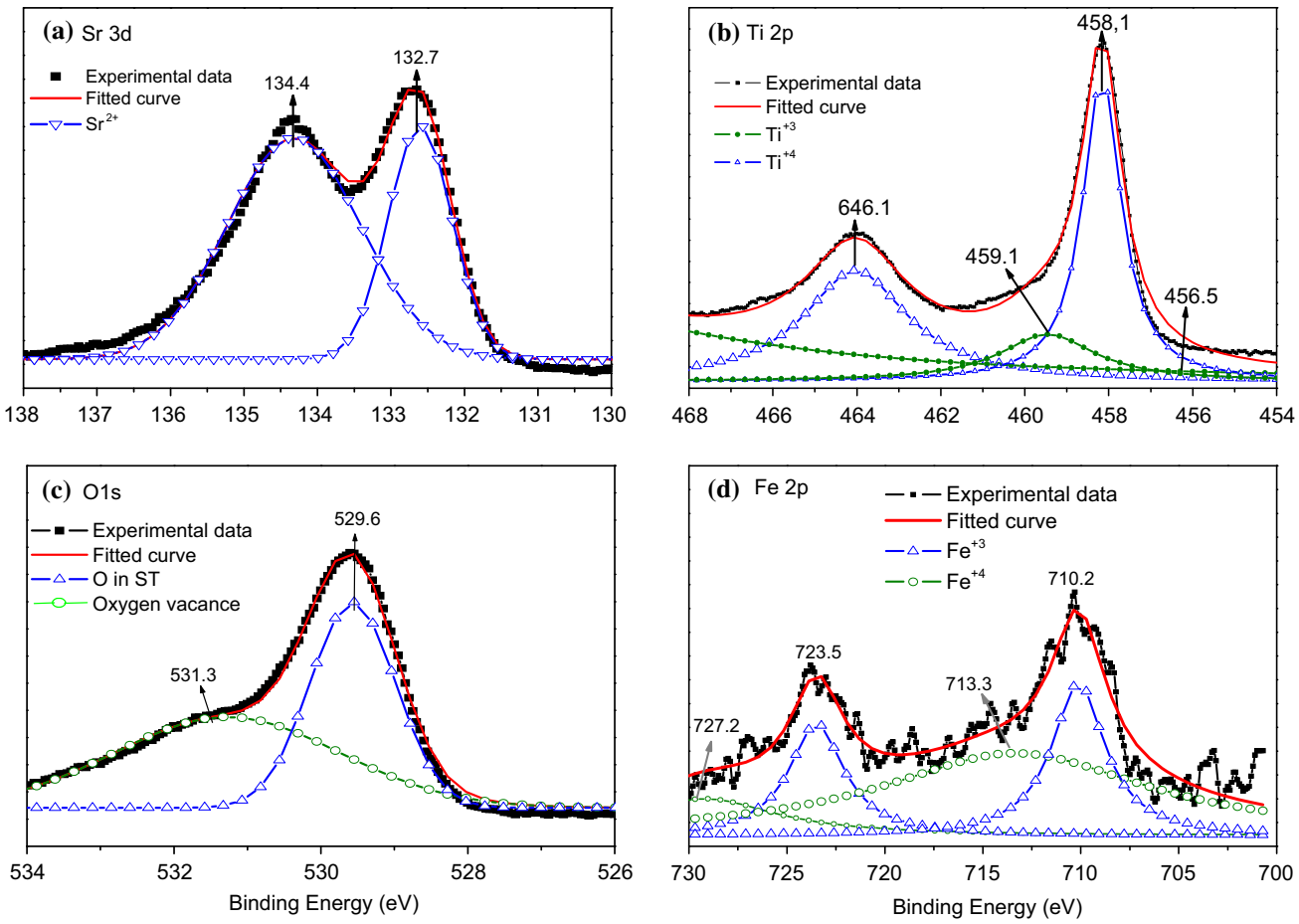

Fig. 2 XPS spectra of the elements for 5 mol% Fe-doped STO sample. **a** Sr 3*d*, **b** Ti 2*p*, **c** O 1s and **d** Fe 3*d*

perovskite structure (space group *Pm3m*) and JCPDS card no 91062-ICSD to measure the lattice parameter. The calculated values of the lattice parameter decreased from 3.916 Å (STO) to 3.899 Å (STO:Fe 3 mol%) due to smaller ionic radius of Fe compared with that of Ti. However, this continuous shift in the XRD spectrum disappears at STO:Fe 5 mol%. This behaviour may be due to the mixture of Fe^{3+} and Fe^{4+} atoms or the strong amorphisation of the structure [26].

3.2 XPS analysis

The STO:Fe samples were analysed by XPS to elucidate their surface chemical characteristics. The oxidation states of the Fe, Sr, Ti and O atoms are shown in Fig. 2. High-resolution core-level scans that were acquired from the XPS spectra for the Sr 3*d*, Ti 2*p*, Fe 3*d* and O 1*s* levels of the STO:Fe 5 mol% sample are shown in Fig. 2a–d. The binding energy positions of the Sr 3*d*-doublet lines at 132.7 and 134.4 eV are due to Sr $3d_{5/2}$ and Sr $3d_{3/2}$, respectively (Fig. 2a), which these values correspond to α-Sr in strontium [27]. Here, the α-component corresponds to Sr atoms in the 'perovskite-like superconductor phase' of the STO:Fe structure.

The binding energies of Ti $2p_{3/2}$ and Ti $2p_{1/2}$ for the STO:Fe samples are 458.1 and 464.0 eV, as shown in Fig. 2b, and are close to the reported values of α-Ti atoms for Ti atoms in the perovskite structure of STO and correspond to Ti with an oxidation state of 4+ [27]. The binding energies of the weak peaks at 456.5 ($2p_{3/2}$) and 459.1 eV ($2p_{1/2}$) were due to Ti^{3+} ions. These ions correspond to a Ti_2O_3 (Ti^{3+}) compound, which is related to a non-perovskite structure of the STO:Fe structure.

As shown in Fig. 2c, the binding energy positions of the O 1*s* spectra yield two peaks. The stronger peak is associated with O^{2-} ions at 529.6 eV, which is related to oxygen in the perovskite structure of STO:Fe, indicating that the oxygen ions remain coordinated in TiO_6 octahedra [27]. The peak at 531.3 eV was due to an intermediate oxidation state for oxygen [i.e. O^{-x} $(0 < x < 2)$] and may be related to carbonate compounds as well as to defect, such as oxygen vacancies and chemical adsorption [28]. The O^{-x} oxidation state is due to oxygen in the non-perovskite structure of STO:Fe [27].

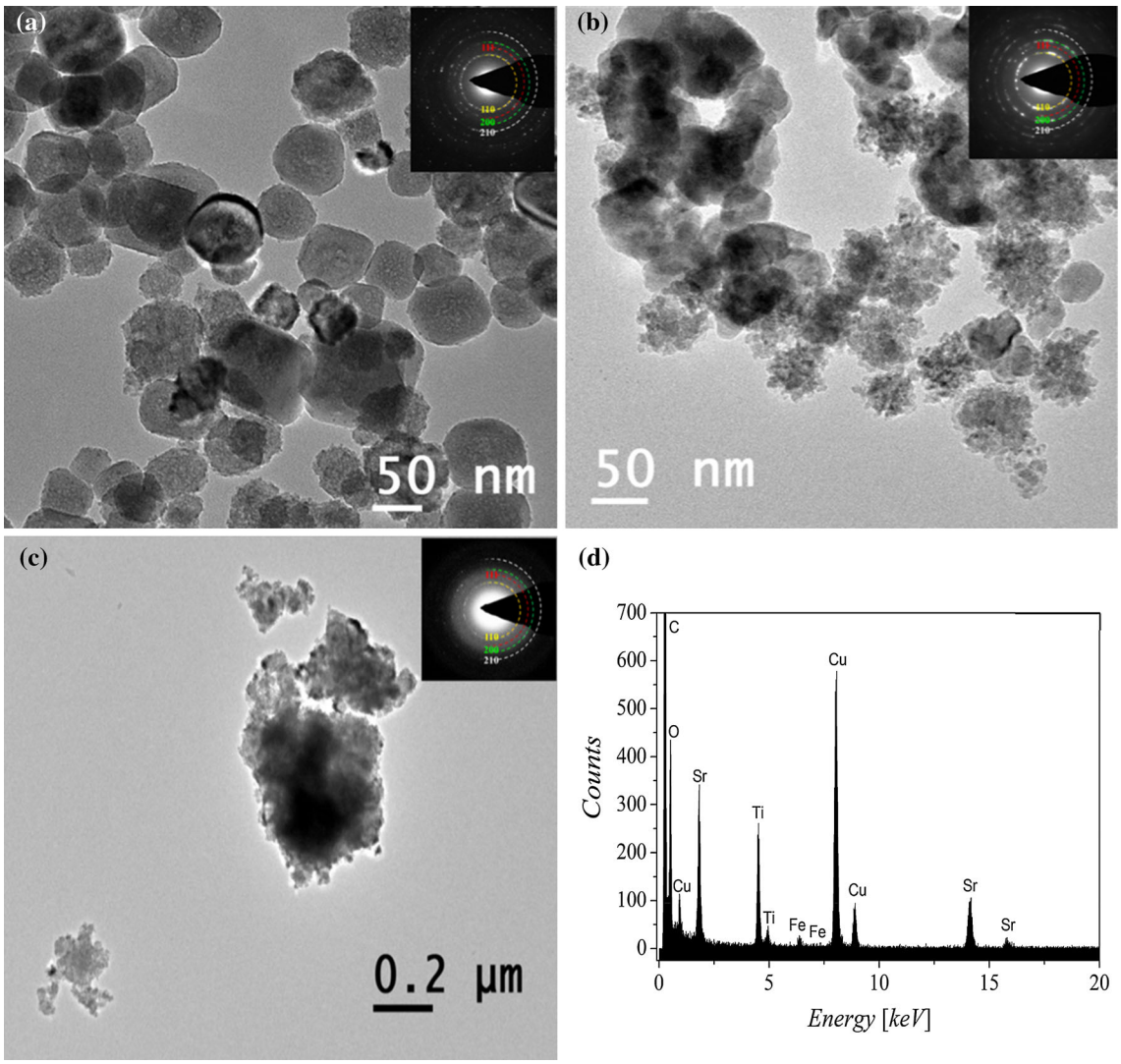

Fig. 3 TEM micrographs and SAED patterns of STO doped with different content of Fe: **a** 1, **b** 3, **c** 5 mol% and **d** corresponding to EDX for the 5 mol% sample. The *colour rings* in each SAED patterns are for guides to the eye (Color figure online)

The Fe 2*p* XPS region, which contains a doublet of $2p_{3/2}$ and $2p_{1/2}$, is shown in Fig. 2d. The peaks are located at 710.2 eV (Fe $2p_{3/2}$) and 723.5 eV (Fe $2p_{1/2}$), which are similar to those reported in a recent study of Fe 2*p* corresponding to the presence of Fe^{3+} [29]. The second doublet was located at 713.3 eV (Fe $2p_{3/2}$) and 727.2 eV (Fe $2p_{1/2}$) and assigned to Fe^{4+} [30, 31]. Therefore, Fe^{3+} and Fe^{4+} ions substitute for Ti in the structure [32].

Bocquet et al. [30] investigated the electronic structure of the Fe^{4+} perovskite oxide $SrFeO_3$ by XPS and concluded that the large increase in charge at the Fe site led to a chemical shift to a higher binding energy. In an XPS study, Ghaffari et al. reported that iron in the STO:Fe perovskite structure participated as a mixture of Fe^{3+} and Fe^{4+} ($SrTi_{(1-x)}[Fe^{3+}, Fe^{4+}]_{(x)}O_{(3-\delta)}$). In an separate report, an increasing Fe content resulted in a significant increase in the amount of Fe^{3+} and Fe^{4+}, resulting in the formation of oxygen vacancies [31].

The presence of the O^{-x} state in the sample is consistent with the XRD results because an increasing Fe concentration in the samples results in poorer crystallinity (i.e. increased amorphisation), which may be due to different defects in the network, such as oxygen vacancies, and the chemical adsorption process.

3.3 Transmission electron microscopy

The morphology of the STO:Fe sample was investigated by low-magnification TEM and EDX, as shown in Fig. 3a–d. The Fe-doped ST nanoparticles are nearly spherical with an average diameter of 100, 200 and 600 nm at 1, 3 and 5 mol% STO:Fe, respectively. 1 mol% Fe results provide

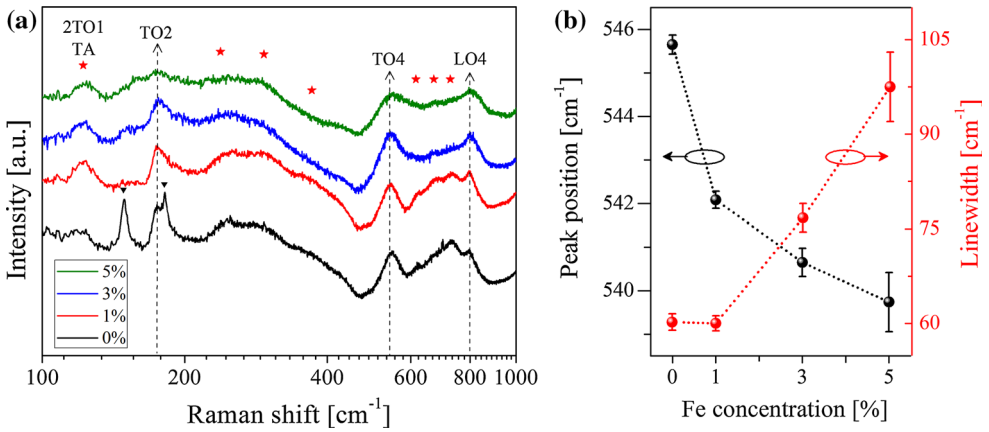

Fig. 4 **a** Room temperature Raman spectra of Fe-doped STO nanoparticles showing peaks associated with first-order scattering processes involving TO_2, TO_4 and LO_4 phonons modes, peaks marked with *star* correspond to the second-order phonons, and peaks marked with *triangle* correspond to traces of $SrCO_3$. **b** Linewidth (*red circles*) and frequency (*black circles*) of TO_4 phonon mode as a function of Fe content. The position and the linewidth were determined by fitting with Lorentzian line shape. The *black* and the *red dotted lines* are for guides to the eye (Color figure online)

better definition of the nanoparticles with spherical shape and defined contours. In addition, these nanoparticles do not appear to agglomerate, as shown in Fig. 3a.

With an increasing concentration of the dopant ion, the definition of the nanoparticles becomes worse and the nanoparticles exhibit irregular agglutination and become difficult to differentiate (Fig. 3b, c). The average diameter of samples increased due to the emergence of the amorphous phase at higher Fe concentrations.

The EDX result shown in Fig. 3d indicates that the 5 mol% sample only contains the Sr, Ti, O and Fe elements in the sample. The results from the TEM analysis are in agreement with those obtained from the XRD analysis, where at higher Fe concentrations, the amorphous phase increases results in less crystallinity. The insets in Fig. 3a, b, c show the SAED patterns for 1, 3 and 5 mol% STO:Fe, respectively. The sharp and decreasing intensity of peaks was observed when the doped Fe content are increased, which indicates that the crystallinity of the samples was lost as the iron content increased,

3.4 Raman spectroscopy

At room temperature, STO single crystals have an ideal cubic perovskite structure (space group: *Pm3m*). Due to the odd symmetry of all of the zone-centre optical phonons, no first-order Raman activity is expected based on group symmetry analysis. Therefore, the room temperature spectrum should be dominated by second-order scattering [33]. However, Raman scattering studies of STO have shown that first-order Raman scattering can actually be observed when the central symmetry is broken due to various factors, such as strain effects, the presence of impurities and defects and oxygen vacancies [34]. For the STO nanoparticles, the origin of symmetry breaking comes from frozen surface dipoles or from local tetragonal arrangement as well as the presence of nanoscopic polar domains due to the incorporated impurities [35].

The room temperature Raman spectra of the STO:Fe nanoparticles with a spectral resolution higher than 0.4 cm^{-1} are shown in Fig. 4a. By comparing these Raman spectra with the published data [24, 33–39], three first-order phonon modes were identified at approximately 171, 540 and 800 cm^{-1} corresponding to the TO_2, TO_4 and LO_4 modes, respectively. The frequencies of the TO_2 and TO_4/LO_4 modes have been determined by fitting with Fano and Lorentzian line shapes, respectively.

The pronounced Fano-like asymmetric line shape of the TO_2 polar mode suggests that the activation of this first-order process is most likely due to the presence of defect-induced ferroelectric polar regions in the nanoparticles [35]. This Fano-like behaviour has been observed in other perovskite nanoparticles [35, 36] and thin films [34, 40–42].

The weak peaks marked with a star at 120 cm^{-1} and between 200 and 400 and 600–800 cm^{-1} were identified as second-order scattering involving two-phonon processes. The peaks marked with a black triangle at approximately 148 and 181 cm^{-1} correspond to trace amounts of $SrCO_3$, which is typically not detected by XRD [36].

Figure 4a shows that with an increasing Fe content, the Raman scattering peaks exhibit a strong decrease in intensity and become broader. Similar results were reported by Van Minh et al. for STO:Fe nanoparticles with Fe concentrations higher than 10 % [24]. In addition, a strong decay in the Raman intensities and overall modification of

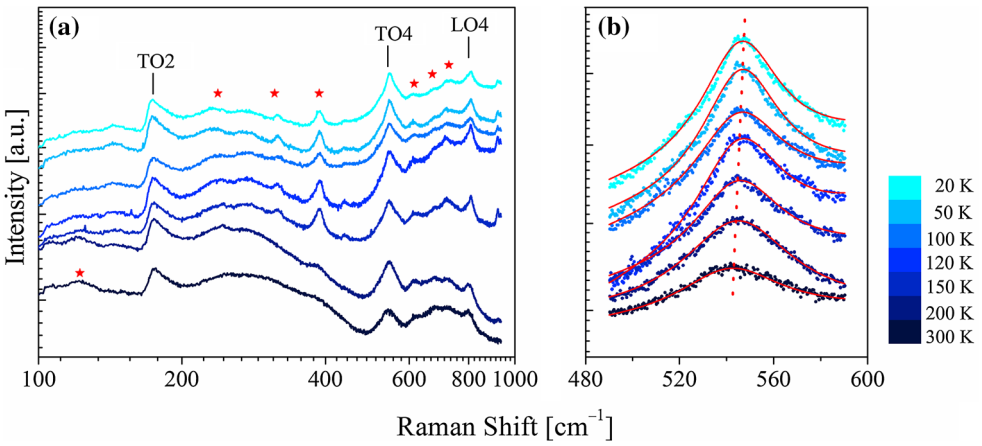

Fig. 5 **a** Temperature evolution of the Raman spectra of STO:Fe 1 mol%. The peaks with *star* correspond to the second-order processes. **b** Temperature dependence of the TO_4 phonon mode. The Raman spectra are denoted by *blue dots,* and the Lorentzian fits are shown in *red solid lines*. All spectra are plotted in the same scale with a small offset for clarity (Color figure online)

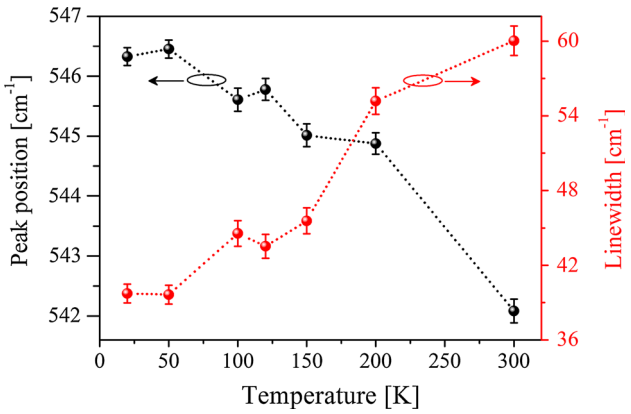

Fig. 6 Temperature dependence of the position TO_4 phonon frequency (*black dots* and *dashed line*) and linewidth (*red dots* and *dashed line*) of STO:Fe 1 % mol. Both parameters were determined by a Lorentzian fit (as shown by the *red lines* in Fig. 5b) (Color figure online)

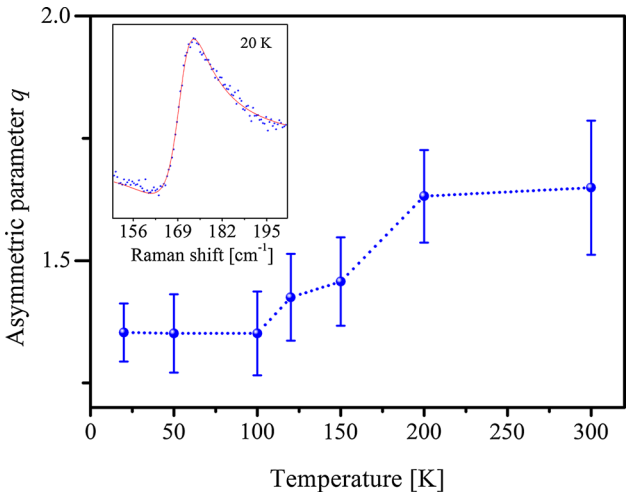

Fig. 7 Temperature dependence of the asymmetry parameter q for STO:Fe 1 % mol (*blue dots*), the values were determined by fitting the Fano line shape to Eq. (1). The *blue dashed line* is used as guide to the eye. *Inset* Fano line shape of the TO_2 phonon mode of STO:Fe 1 % mol at 20 K (*blue dots*), the *red line* corresponds to the Fano profile fitted by using Eq. (1) (Color figure online)

the Raman spectra was observed as the Fe concentration increased. Van Minh et al. attributed this effect to disorder and compositional fluctuations induced by the random distribution of Ti and Fe atoms in the B-site in the ABO_3 sublattices. This effect will destroy the translational invariance, leading to symmetry breaking and corresponding changes in the Raman spectrum.

The effect of the Fe concentration on the TO_4 phonon modes is shown in Fig. 4b. A marked shift to lower frequencies and a broadening of the linewidth (full width at half maximum, FWHM) were observed as the Fe concentration increased. Based on the difference in the atomic weights of the Ti (47.88) and Fe (55.85) atoms, the lower frequency shift can be explained by the simple mass effect [phonon frequency $\sim(k/m)^{1/2}$, where k is the force constant and m the weight] and the weaker bonds due to the amorphisation with increasing the Fe content.

The Raman spectra and a close up of the TO_4 mode for STO:Fe 1 mol% as a function of temperature from 20 to 300 K are shown in Fig. 5. The results in Figs. 5b and 6 indicate that as the temperature decreased, a strong blue shift in the frequency and sharpening of the FWHM of the TO_4 mode were observed. These two related effects arise because an increase in the temperature (decrease) displaces the atoms from their equilibrium positions, resulting in an overall volume expansion or contraction of the lattice and a change in the interatomic forces due to the anharmonicity of the bonds. This change in the interatomic force is reflected in the Raman frequencies, which shift to lower frequencies as the temperature increases. Similarly, the linewidth becomes broader with increasing temperature due to the temperature dependence of the phonon lifetime. This temperature dependence of the Raman signal can be used as a fingerprint to probe the thermal properties of the material [43, 44].

The temperature dependence of the Fano asymmetry parameter (q) of the TO_2 mode is shown in Fig. 7. The Fano-like shape was fitted using:

$$I(\omega) = \frac{A(q + E(\omega))^2}{1 + E(\omega)^2} + C \quad (1)$$

where $E(\omega)$ is the reduced frequency given by

$$E(\omega) = 2(\omega - \omega_0)/\Gamma \quad (2)$$

and $I(\omega)$ is the intensity, A is the amplitude, ω_0 is the phonon frequency, q is the Fano asymmetry parameter, Γ is the FWHM, and C is a constant that accounts for the background signal. Positive values of q indicate that the scattering intensity is greater on the high-energy side of the peak. In contrast, negative values of q indicate the interference with the electronic continuum [35]. The q parameter did not exhibit significant temperature dependence, confirming the results reported by Rabuffetti et al. [36] for STO nanocubes. However, this result is different from the results reported by Banerjee et al. [35], who reported an oscillating temperature dependence of q in similar nanostructures. This controversial behaviour remains unclear, and more research is needed.

4 Conclusions

In summary, nanocrystalline $SrTi_{(1-x)}O_3$:Fe_x powders with $x = 0$, 1, 3 and 5 mol% Fe were synthesised by a sol–gel hydrothermal process to study doping effects on the structure using X-ray photoelectron and Raman scattering spectroscopy.

The XRD and Raman results indicate that the Fe-doped STO nanoparticles have a cubic perovskite structure for all of the Fe-doping contents with no evidence of a secondary phase. However, XRD indicated that at higher Fe concentrations, the materials primarily exhibit an amorphous phase with a very small degree of crystallisation, which is in agreement with the TEM images. In fact, with an increasing percentage of dopant ions, the crystalline definition of the nanoparticles is lost and the nanoparticles exhibit agglutination. The XPS results indicated that Sr ions were in the 2+ oxidation state, and in the perovskite structure, Fe participated as a mixture of Fe^{3+} and Fe^{4+}, which significantly increased the formation of oxygen vacancies as the Fe content increased.

The presence of a Fano-like asymmetric line shape in the TO_2 phonon mode suggested that the activation of the first-order Raman active modes at room temperature may be due to the presence of a defect-induced ferroelectric polar region in the nanoparticles. The Fe content dependence of the TO_4 phonon mode suggests that this mode can be used as a fingerprint of the Fe content in slightly doped STO nanoparticles. Similarly, the temperature dependence of the TO_4 phonon mode of the 1 mol% Fe-doped sample also suggests that it could be used as an ideal fingerprint to probe the thermal properties of the sample.

Acknowledgments The authors acknowledge the financial support from the FONDECYT grant under contract No. 1110555, the basal Financing program CONICYT FB0807 (CEDENNA). ECA and CMST gratefully acknowledge financial support from the Spanish MINECO projects nanoTHERM (Grant No. CSD2010-0044) and TAPHOR (MAT2012-31392), as well as partial support from the Severo Ochoa Program (MINECO, Grant SEV-2013-0295).

References

1. Tejuca LJ, Fierro JLG (1993) Properties and applications of perovskite-type oxides. CRC Press, New York
2. Müller K, Burkard H (1979) $SrTiO_3$: an intrinsic quantum paraelectric below 4 K. Phys Rev B 19:3593
3. Eisenbeiser K, Finder JM, Yu Z, Ramdani J, Curless JA, Hallmark JA (2000) Field effect transistors with $SrTiO_3$ gate dielectric on Si. Appl Phys Lett 76:1324
4. Först CJ, Ashman CR, Schwarz K, Blöchl PE (2004) The interface between silicon and a high-k oxide. Nature 427:53
5. Ohta S, Nomura T, Ohta H, Hirano M, Hosono H, Koumoto K (2005) Large thermoelectric performance of heavily Nb-doped $SrTiO_3$ epitaxial film at high temperature. Appl Phys Lett 87:092108
6. Kan D, Terashima T, Kanda R, Masuno A, Tanaka K, Chu S (2005) Blue-light emission at room temperature from Ar irradiated $SrTiO_3$. Nat Mater 4:816
7. Ohta H (2007) Thermoelectrics based on strontium titanate. Mater Today 10:44
8. Choi M, Oba F, Kumagai Y, Tanaka I (2013) Anti-ferrodistortive-like oxygen-octahedron rotation induced by the oxygen vacancy in cubic $SrTiO_3$. Adv Mater 25:86
9. Gao F, Yang S, Li J, Qin M, Zhang Y, Sun H (2015) Fabrication, dielectric, and thermoelectric properties of textured $SrTiO_3$ ceramics prepared by RTGG method. Ceram Int 41:127
10. Zhang Z, Zhao L, Wang X, Yang J (2004) The preparation and electrical properties of $SrTiO_3$-based capacitor-varistor double-function ceramics. J Sol-Gel Sci Technol 32:367
11. Ghaffari M, Huang H, Tan PY, Tan OK (2012) Synthesis and visible light photocatalytic properties of $SrTi_{(1-x)}FexO_{(3-\delta)}$ powder for indoor decontamination. Powder Technol 225:221
12. Yan JH, Zhu YR, Tang YG, Zheng SQ (2009) Nitrogen-doped $SrTiO_3/TiO_2$ composite photocatalysts for hydrogen production under visible light irradiation. J Alloys Compd 472:429
13. Rüdiger A, Schneller T, Roelofs A, Tiedke S, Schmitz T, Waser R (2005) Nanosize ferroelectric oxides—tracking down the superparaelectric limit. Appl Phys A 80:1247
14. Wu X, Wu D, Liu X (2008) Negative pressure effects in $SrTiO_3$ nanoparticles investigated by Raman spectroscopy. Solid State Commun 145:255
15. Wang Y, Chen J, Wu X (2001) Preparation and gas-sensing properties of perovskite-type $SrFeO_3$ oxide. Mater Lett 49:361
16. Zhang Y, Hu J, Cao E, Sun L, Qin H (2012) Vacancy induced magnetism in $SrTiO_3$. J Magn Magn Mater 324:1770
17. Kazan S, Şale AG, Gatiiatova JI, Valeev VF, Khaibullin RI, Mikailzade FA (2010) Magnetic resonance and ferromagnetic behaviour in Fe-implanted. Solid State Commun 150:219

18. Van Minh N, Phuong DTT (2011) $SrTi_{(1-x)}Fe_xO_3$ nanoparticle: a study of structural, optical, impedance and magnetic properties. J Exp Nanosci 6:226
19. Sendilkumar A, Raju KCJ, Babu PD, Srinath S (2013) Positive temperature coefficient of resistance of tetragonal Ti^{4+} doped nano $SrFeO_{3-\delta}$. J Alloys Compd 561:174
20. Moos R, Menesklou W, Schreiner H-J, Härdtl KH (2000) Materials for temperature independent resistive oxygen sensors for combustion exhaust gas control. Sensors Actuators B Chem 67:178
21. Neri G, Bonavita A, Micali G, Rizzo G, Licheri R, Orru R (2007) Resistive λ-sensors based on ball milled Fe-doped $SrTiO_3$ nanopowders obtained by self-propagating high-temperature synthesis (SHS). Sensors Actuators B Chem 126(1):258. doi:10.1016/j.snb.2006.12.008
22. Xu J, Wei Y, Huang Y, Wang J, Zheng X, Sun Z, Fan L, Wu J (2014) Solvothermal synthesis nitrogen doped $SrTiO_3$ with high visible light photocatalytic activity. Ceram Int 40:10583
23. Selmi F, Ghodgaonkar DK, Hughes R, Varadan VV, Varadan VK (1991) Ceramic phase-shifters for electronically steerable antenna systems. In: Breakwell J, Varadan VK (eds) Proceedings of SPIE 1489, structures sensing and control:97
24. Van Minh N, Phuong DTT (2010) Dopant effects on the structural, low temperature Raman scattering and electrical transport properties in $SrTi_{(1-x)}FexO_3$ nanoparticles synthesized by sol-gel method. J Sol-Gel Sci Technol 55:255
25. Lenser C, Kalinko A, Kuzmin A, Berzins D, Purans J, Szot K (2011) Spectroscopic study of the electric field induced valence change of Fe-defect centers in $SrTiO_3$. Phys Chem Chem Phys 13:20779
26. Verma AS, Kumar A, Bhardwaj SR (2008) Correlation between ionic charge and the lattice constant of cubic perovskite solids. Phys Status Solidi 245:1520
27. Ehre D, Cohen H, Lyahovitskaya V, Lubomirsky I (2008) X-ray photoelectron spectroscopy of amorphous and quasiamorphous phases of $BaTiO_3$ and $SrTiO_3$. Phys Rev B 77:184106
28. Merino NA, Barbero BP, Eloy P, Cadús LE (2006) $La_{1-x}Ca_{x}CoO_3$ perovskite-type oxides: identification of the surface oxygen species by XPS. Appl Surf Sci 253:1489
29. Ghaffari M, Liu T, Huang H, Tan OK, Shannon M (2012) Investigation of local structure effect and X-ray absorption characteristics (EXAFS) of Fe(Ti) K-edge on photocatalyst properties of $SrTi_{(1-x)}FexO_{(3-\delta)}$. Mater Chem Phys 136:347
30. Bocquet A, Fujimori A, Mizokawa T, Saitoh T, Namatame H, Suga S (1992) Electronic structure of $SrFe_4O_3$ and related Fe perovskite oxides. Phys Rev B 45:1561
31. Ghaffari M, Shannon M, Hui H, Tan OK, Irannejad A (2012) Preparation, surface state and band structure studies of $SrTi_{(1-x)}Fe_{(x)}O_{(3-\delta)}$ (x = 0–1) perovskite-type nano structure by X-ray and ultraviolet photoelectron spectroscopy. Surf Sci 606:670
32. Sahner K, Schönauer D, Moos R, Matam M, Post ML (2006) Effect of electrodes and zeolite cover layer on hydrocarbon sensing with p-type perovskite $SrTi_{0.8}Fe_{0.2}O_{3-\delta}$ thick and thin films. J Mater Sci 41:5828
33. Balachandran U, Eror NG (1982) Raman spectra of strontium titanate. J Am Ceram Soc 65:c54
34. Sirenko A, Akimov I, Fox J, Clark A, Li H-C, Si W (1999) Observation of the first-order Raman scattering in $SrTiO_3$ thin films. Phys Rev Lett 82:4500
35. Banerjee S, Kim D-I, Robinson RD, Herman IP, Mao Y, Wong SS (2006) Observation of Fano asymmetry in Raman spectra of SrTiO3 and $CaxSr_{(1-x)}TiO_3$ perovskite nanocubes. Appl Phys Lett 89:223130
36. Rabuffetti FA, Kim H-S, Enterkin JA, Wang Y, Lanier CH, Marks LD (2008) Synthesis-dependent first-order Raman scattering in $SrTiO_3$ nanocubes at room temperature. Chem Mater 20:5628
37. Zhong W, King-Smith RD, Vanderbilt D (1994) Giant LO–TO splittings in perovskite ferroelectrics. Phys Rev Lett 72:3618
38. Maletic S, Popovic D, Dojcilovic J (2010) Dielectric measurements, Raman scattering and surface studies of Sm-doped $SrTiO_3$ single crystal. J Alloys Compd 496:388
39. Rodenbücher C, Jauß A, Havel V, Waser R, Szot K (2014) Fast mapping of inhomogeneities in the popular metallic perovskite $Nb:SrTio_3$ by confocal Raman microscopy. Phys Status Solidi Rapid Res Lett 08:781
40. Gupta S, Katiyar RS (2001) Temperature-dependent structural characterization of sol–gel deposited strontium titanate ($SrTiO_3$) thin films using Raman spectroscopy. J Raman Spectrosc 32:885
41. Du YL, Chen G, Zhang MS (2004) Investigation of structural phase transition in polycrystalline $SrTiO_3$ thin films by Raman spectroscopy. Solid State Commun 130:577
42. Ostapchuk T, Petzelt J, Železný V, Pashkin A, Pokorný J, Drbohlav I (2002) Origin of soft-mode stiffening and reduced dielectric response in $SrTiO_3$ thin films. Phys Rev B 66:235406
43. Chávez-Ángel E, Reparaz JS, Gomis-Bresco J, Wagner MR, Cuffe J, Graczykowski B (2014) Reduction of the thermal conductivity in free-standing silicon nano-membranes investigated by non-invasive Raman thermometry. APL Mater 2:012113
44. Reparaz JS, Chavez-Angel E, Wagner MR, Graczykowski B, Gomis-Bresco J, Alzina F (2014) A novel contactless technique for thermal field mapping and thermal conductivity determination: two-laser Raman thermometry. Rev Sci Instrum 85:034901